THE PHOTOGRAMMETRIC RECORD

The Photogrammetric Record 31(154): 121–142 (June 2016)
DOI: 10.1111/phor.12149

MONITORING OF A LABORATORY-SCALE INLAND-DELTA FORMATION USING A STRUCTURED-LIGHT SYSTEM

DEVRIM AKCA[1] (akca@isikun.edu.tr)
Isik University, Istanbul, Turkey

HANSJÖRG SEYBOLD[2] (hseybold@mit.edu)
ETH Zurich, Switzerland

[1]*Formerly at Swiss Federal Institute of Technology (ETH), Zurich, Switzerland*
[2]*Formerly at Massachusetts Institute of Technology (MIT), Cambridge, Massachusetts, USA*

(Extended version of a paper presented at the XXIInd ISPRS Congress, held in Melbourne, Australia from 25th August to 1st September 2012)

Abstract

A reduced complexity model, which simulates the process of fluvial inland-delta formation, has been developed in a previous study. The results have been compared and validated with a laboratory experiment. This work elaborates the laboratory investigation in which an experimental inland delta is generated and its eroding topography is measured using a structured-light 3D scanner. The least squares 3D (LS3D) co-registration and comparison method is used for alignment as well as for comparing data epochs both spatially and temporally. A spatial precision value of around ±50 μm (1/20 000) is achieved. A series of high-quality digital elevation models (DEMs) are generated and the space-time evolution of the inland delta is monitored and analysed, in terms of slope and topography dynamics, in the consecutive DEM layers. The combination of high-resolution scanning together with high-precision co-registration techniques allows investigation of the details of the space-time variability of the sedimentation-deposition patterns to be used for geomorphological analysis.

KEYWORDS: co-registration, digital elevation model (DEM), geomorphology, structured-light system, 3D comparison, 3D scanning

INTRODUCTION

THE GEOMORPHOLOGICAL EVOLUTION of a fluvial delta surface is mainly influenced by the dynamics of rivers and their sediment transport capacity, where the interaction with the topography and the material properties of the ground surface play an essential role. The physical models based on hydrological equations and constitutive sediment transport laws

are not applicable as the range of time scales and channel length involved in the delta formation process are too broad to be examined with today's computational power. Thus, new models have to be developed, reducing the complexity of hydrological and sedimentary equations but still keeping the essential physics of the first-order dynamics (Paola and Leeder, 2011). These *reduced complexity models* are concatenated with cellular automata, which require cellular discretisation of ground topography in terms of the digital elevation model (DEM) representation, to model the evolution over time of geophysical processes. The motivation for this type of modelling is not to simulate the deterministic evolution of a given river, but to identify the essential physics of the underlying processes. The results then can be compared and validated with field measurements and laboratory experiments. More information can be found in Bokulich (2013) and Liang et al. (2015).

Seybold et al. (2009) have developed such a reduced complexity model to study the formation of inland deltas, which simulates the process on geological time scales. It combines the simplicity of the cellular automata with the hydrodynamic features to reproduce realistic river delta patterns. The reduced complexity delta model has been validated by applying the results to the Okavango Delta, Botswana (Fig. 1) and the Mississippi Delta, USA (Seybold et al., 2010). This work has been accompanied by a laboratory-scale flume experiment where the morphology of the different sedimentation patterns has been analysed in spatial and temporal domains. The present paper focuses on the 3D measurement, interpolation, co-registration, DEM generation and analysis aspects of this flume experiment.

A micro-scale artificial inland delta was generated under laboratory conditions, with the delta formation process lasting two days. The surface topography was surveyed with a high-accuracy 3D scanner at five data epochs. Each epoch was represented by a separate DEM layer. The consecutive DEMs were analysed in 3D space using the surface co-registration and comparison methods. The technical details of the laboratory set-up and the 3D scanner are given in the next section preceded by a selective review of published close-range morphological measurement works in the earth sciences. The third section comprises the 3D modelling workflow from data acquisition to the high-quality DEM-generation step. The geomorphologic analyses are given in the fourth section. While Seybold et al. (2010) mainly focused on the statistical properties of delta-surface variability and its comparison with real-world deltas (the Okavango and Mississippi deltas), this paper presents laboratory-model data acquisition, geo-processing, formation of stratigraphic layers and analysis of the three-dimensional surface dynamics. Furthermore, it is shown that the high-resolution scanning technique is capable of capturing small-scale features of the experiment such as channel banks or levees.

FIG. 1. The Okavango Delta in Botswana.

Close-range Morphological Measurement in the Earth Sciences

Photogrammetric methods have been used for close-range morphological measurement in the earth sciences for many years, such as for the precise measurement of stream channel erosion (Welch and Jordan, 1983), land-surface roughness and surface slope (Kirby, 1991), river-bank dynamics and erosion (Pyle et al., 1997), soil-surface microrelief in the representation of DEMs (Merel and Farres, 1998), realistic replication of river beds (Chandler et al., 2003), rill erosion (Gessesse et al., 2010), bedrock erosion (Rieke-Zapp et al., 2012) and an artificially generated shallow landslide (Akca, 2013).

Terrestrial laser scanners (TLSs) are versatile devices which are used for rapid and dense point-cloud data acquisition tasks, commonly for 2 to 50 m sensor-to-object distances. For example, they have been used for the computation of erosion and deposition volumes and channel change along riversides (Milan et al., 2007), sedimentological applications (Hodge et al., 2009), geological applications (Buckley et al., 2010), fluvial landform measurement and hydraulic modelling (Hohenthal et al., 2011), geomorphological applications (Brodu and Lague, 2012), determination of river-bed characteristics (Brasington et al., 2012) and quantification of bedrock erosion (Wilson and Lavé, 2013). All these works have been performed under outdoor conditions. Fewer applications are available where the TLS have been used in indoor experiments (Hürlimann et al., 2015; Jouannic et al., 2015).

Photogrammetry and laser scanning are not only competing but also complementary techniques (Remondino, 2011). Scanners are easy to use and reliable in surface modelling due to high data redundancy. However, they are expensive, both in terms of hardware and software, and pose difficulties in logistics and transportation. In contrast, close range photogrammetry has lower hardware costs and is more flexible, yet it requires a certain level of expertise in its operation. Data post-processing is typically more time consuming for photogrammetry as well. The question of which is the better choice for a certain project has been discussed by Chandler (2010), concluding that it depends on the task, budget and expertise.

Indoor flume experiments in laboratory conditions have often been carried out using close range photogrammetry in the past. Stojic et al. (1998) achieved a precision for automatically generated DEMs within the range of $\pm 0{\cdot}5$ to $\pm 1{\cdot}7$ mm using a Pentax 645 non-metric camera. Chandler et al. (2001) successfully studied a Kodak DCS460 digital camera to generate dense DEMs representing a flume surface. Comparisons showed that accuracies of $\pm 2{\cdot}5$ mm have been achieved at independent check points with a camera-to-object distance of 4·2 m. Rieke-Zapp and Nearing (2005) used a Kodak DCS1 digital camera to generate a total of 60 DEMs covering a planimetric area of 16 m^2. They attained a precision of $\pm 1{\cdot}26$ mm in the vertical direction. Heng et al. (2010) used two 10-megapixel Nikon D80 digital SLR cameras to generate a digital surface model (DSM) of a flume surface measuring 1·4 m by 3·9 m. They found a precision of $\pm 2{\cdot}59$ mm, on average, by comparing DEMs of the same surface extracted from different image pairs. They also compared a photogrammetrically derived DEM with one acquired with a Leica ScanStation 2 TLS, which provides a difference map with a mean of $-0{\cdot}92$ mm and a standard deviation of $\pm 3{\cdot}50$ mm. Berger et al. (2010) performed an experiment to study how rill networks are initiated and then evolve over time under controlled laboratory conditions. They used an ALPA 12 TC camera in stereo-image acquisition mode. Triangulation and point positioning were performed using a bundle adjustment and DEMs were calculated, but no precision value was reported. Kraal et al. (2008) studied the formation of alluvial fans caused by rapid water release. In another laboratory experiment, Bonnet (2009) studied shrinking and splitting mechanisms of drainage basins. In both of these works photogrammetric measurement details and quality figures were not given.

With recent advances in 3D sensor technology, structured-light systems have become an alternative way of performing 3D point-cloud measurement tasks in laboratory flume experiments. They are effective for sensor-to-object distances up to 1 m. The following studies used such scanner systems. Bonnet and Crave (2003) generated laboratory-scale terrain topography and analysed its evolution by erosion. Babault et al. (2005) studied relief dynamics using laboratory-scale models submitted to uplift under runoff-driven erosion. Turowski et al. (2006) performed a series of experiments to investigate the relationship between channel geometry and tectonic forcing in steady-state landscapes at various uplift rates. Both Hoyal and Sheets (2009) and Martin et al. (2009) designed and realised laboratory flume experiments to study delta formation. All these papers focused on geomorphic patterns; none of them reported the technical capabilities of the scanners used or their pre- and post-processing steps. The technical approaches of surface measurement, point-cloud processing and DEM-generation steps indeed played an important role, even though they are barely discussed in these papers.

The aforementioned research activities and achievements demonstrate the relevance of the present study. It is apparent that high-quality DEMs, in terms of resolution and accuracy, are essentially required in earth science studies. Delta formation is a temporal process, which can be covered in sequential DEM layers each of which is designated to represent a certain time slot. Not only the generation of DEMs but also their co-registration and comparison issues are important. In this paper the essential steps of the DEM processing pipeline are exhaustively discussed, including measurement design and realisation, point-cloud acquisition, spatial and temporal co-registration, surface interpolation and mesh generation, 3D comparison and visualisation. In addition, appropriate precision values are reported. Special attention has been given to the unique co-registration and comparison algorithm based on the least squares 3D (LS3D) surface-matching method (Gruen and Akca, 2005; Akca, 2010) whose output was used in the analysis. It is also demonstrated how DEM-related information is used for slope analysis and topography dynamics.

FLUME EXPERIMENT

Laboratory Set-up

The set-up of the flume experiment discussed in Seybold et al. (2010) consisted of a 1 m × 1 m aluminium basin, which was fixed at an inclination of about 6° (Fig. 2). The main slope ran along the diagonal of the basin. An initial surface was created using a uniformly sloped sediment layer with a height of 5 cm at the inlet (Figs. 2(a) and (b)). The sediment consisted of crushed glass with a diameter of 50 to 120 μm and has a bulk density of $\rho = 2{\cdot}2\ \mathrm{g/cm^3}$. Note that the focus here is only on the dry experiment of Seybold et al. (2010).

A sediment–water mixture was injected at the upper end of the flume at a constant rate using a peristaltic pump (Pump1 in Fig. 2). The sediment concentration was kept constant during the injection period by continuously stirring the mixture in an upstream tank (Fig. 2) with a marine-type impeller. The volumetric sediment concentration was approximately 5% and the inflow rate was set to 1000 ml/h. To model the boundary conditions of a dry delta, infiltrated water which seeped out at the bottom edge of the flume was continuously pumped out (Pump2 in Fig. 2) to avoid the formation of a lake downstream of the edge of the delta lobe.

In order to dry the surface and additionally evaporate water, an array of fifteen 300-watt heat lamps were fixed 15 cm above the surface (Fig. 3). According to empirical tests, they are capable of fully evaporating the water and moisture content of the basin in 2 h.

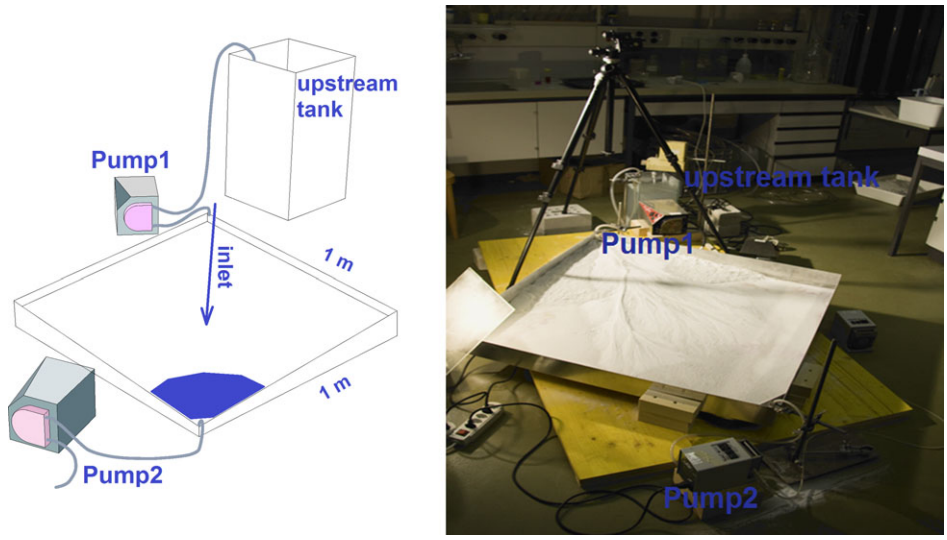

(a) (b)

FIG. 2. The flume experiment set-up.

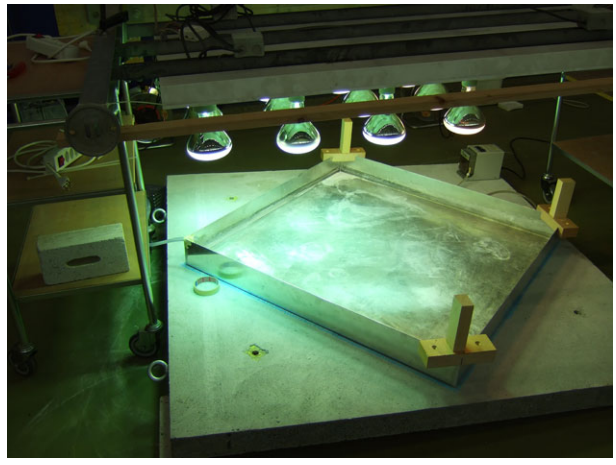

FIG. 3. The heating lamps above the delta model.

The experiment was run as follows. The sediment–water mixture was injected into the flume over a 45-min period, followed by drying of the flume surface over 2 h 15 min. One period of injection and drying is termed an "epoch" in this study, with epoch 0 denoting the initial condition. After complete drying by the end of each epoch, the surface topography was scanned using a Breuckmann optoTOP-SE 3D scanner (see the next section). Data for five epochs were collected: epochs 0 to 4. Complete drying is necessary to avoid specular

reflections produced by wet sand; these reflections would otherwise disturb the scanning procedure by decreasing the accuracy and causing voids in the point cloud (see Fig. 6(a)).

Breuckmann OptoTOP-SE 3D Scanner

A Breuckmann optoTOP-SE system was used for the surface measurements (Fig. 4). This is a topometrical 3D scanner, allowing three-dimensional digitisation of objects with high resolution and accuracy. The scanner uses a coded structured-light system, in which regular fringes (black and white stripes) are projected onto the object surface and the stripes' deformations are measured using a charge-coupled device (CCD) camera. From the deformations of these stripes the topography can be reconstructed with an accuracy of $\pm 50\,\mu m$ for typical objects whose surface reflectivity is diffuse, such as wood, concrete, paper, stone or similar materials (Akca, 2012). The technical specifications of the system are given in Table I.

The 3D object point coordinates are computed by employing the photogrammetric triangulation (spatial ray intersection) principle based on the projector and camera calibration information. The 2D coordinates of the projector and the camera's homologous points are automatically matched by adopting an appropriate codification strategy, such as black-and-white fringe stripes, continuously varying colour codes, colour-coded stripes or pseudo-random binary dots (Salvi et al., 2010; Geng, 2011).

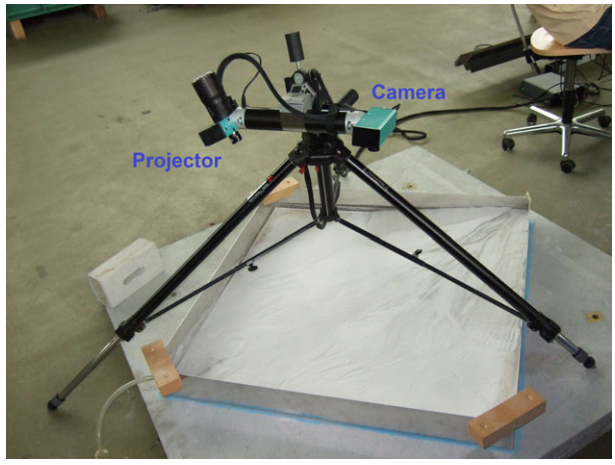

FIG. 4. Breuckmann optoTOP-SE scanner.

TABLE I. Technical specifications of Breuckmann optoTOP-SE scanner.

Field of view	400 mm × 315 mm	Acquisition time	<1 s
Depth of view	260 mm	Digitisation	1280 × 1024 points
Weight	2 to 3 kg	Triangulation angle	30°
Base length	300 mm	Projector pattern	128 order sinus
Lamp	100-watt halogen	Lateral resolution	300 µm
		Feature accuracy	50 µm

The sensor can be scaled to accommodate a wide range of field of views (FOVs) by changing the baseline distance and/or lenses, typically between a few centimetres up to several metres. Thus, the specifications of the sensor can be adapted to the demands of a given measuring task. The time for a single scan takes about 1 s for a 1·4-megapixel camera. State-of-the-art structured-light scanners are equipped with 16-megapixel digital cameras and are still able to take a single scan in about 1 s. This configuration leads to the attainment of a larger FOV or a denser point cloud. In its highest precision mode, the point resolution approaches a 10 to 20 μm inter-point distance. When selecting a 3D scanner, there are trade-offs between specific application requirements and key performance parameters such as precision, reliability, resolution, FOV, flexibility, volume, portability, ease of use, operational speed, calibration conditions and cost.

3D Modelling

The 3D modelling workflow comprises scanning, co-registration, interpolation, surface generation, editing, comparison and visualisation. These steps are outlined below.

3D Scanning

The Breuckmann optoTOP-SE is a very light and flexible 3D scanning system. It can easily be oriented towards the object of interest using a stable tripod. Since the system has only a 400 mm × 315 mm FOV for the best scanner-to-object viewing angle, several scans have to be performed in order to cover the entire 1 m × 1 m object in this research. Thus, planning the scan point-cloud overlays needs careful preparation. The flume area of each epoch was considered as one block and covered by three adjacent scan strips. Each strip had three to five scans with 30 to 40% sidelap (lateral overlap between the strips) and a similar endlap (forward overlap between the intra-strip scans). In total, 13 to 15 point clouds were scanned for each epoch (Table II). This strategy provided optimal data coverage weighed against scanning effort.

Each point cloud consisted of 1280 × 1024 = 1 310 720 points with X, Y, Z and intensity values. The average point spacing was 35 μm in all datasets. The scanning step of a single epoch took 1 to 2 h of working time. The whole experiment with five epochs lasted two days.

Table II. Numerical results of the co-registrations of the intra-epoch point clouds.

Epoch	*Number of point clouds*	*Number of pairwise registrations*	*Mean overlap between the pairwise registrations (%)*	*Minimum overlap between the pairwise registrations (%)*	*Mean standard deviation of the pairwise registrations (μm)*	*Standard deviation of the global registration[a] (μm)*
Epoch 0	14	24	37·7	3·7	68·3	42·4
Epoch 1	13	22	37·9	13·4	53·4	34·0
Epoch 2	13	22	30·8	8·8	52·6	34·6
Epoch 3	14	28	31·7	11·4	53·7	32·2
Epoch 4	15	33	27·2	7·2	46·4	42·7

[a]Standard deviation of the unit weighted observation of the final block adjustment by independent models.

Co-registration of Intra-epoch Scans

The individual scans (in the form of point clouds) have to be combined into a co-registered mosaic to cover the entire surface of the related epoch. Several alignment options are available. The iterative closest point (ICP) method (Besl and McKay, 1992; Chen and Medioni, 1992; Zhang, 1994) and its variants (Gruen and Akca, 2005) are the most popular methods. However, in this research the LS3D surface-matching method was adopted (Gruen and Akca, 2005; Akca, 2010). The LS3D method is a rigorous algorithm for the matching of overlapping 3D surfaces and/or point clouds. It estimates the transformation parameters of one or more fully 3D surfaces with respect to a template surface, using the generalised Gauss–Markov model and thus minimising the sum of the squares of the Euclidean distances between the surfaces. This formulation provides the opportunity to match arbitrarily oriented 3D surfaces without using explicit tie points. It is a powerful method whose accuracy and precision potential is directly dependent on the quality of the input data. For instance, the standard deviation of a pairwise co-registration of two point clouds acquired by a Breuckmann stereoSCAN system was reported by Akca (2007) as $\pm 11{\cdot}3\,\mu m$. This figure provides an indication of the system's precision.

In the LS3D approach when more than two point clouds with multiple overlaps exist, as in the case of this experiment, a two-step solution should be adopted. This consisted of two steps in this study. In the first step, pairwise LS3D matching was performed on every overlapping pair and a subset of point correspondences was saved to a separate, individual file. In the following global registration step, all these files were passed to a block adjustment using the independent models procedure, in which all residual errors are evenly distributed among all the point clouds. Details of the procedure can be found in Akca (2010).

The LS3D method was preferred over the more common ICP in this special experiment because of the following advantages:

(1) LS3D is based on a rigorous mathematical model which can co-register datasets with little surface information. The flume surface with its rare curvature and almost flat topography in some parts is an example of this peculiar case.
(2) LS3D can accomplish a successful co-registration, even though the overlap between the surface pairs is minimal, such as the 3·7% overlap given in Table II.
(3) Due to its quadratic type of convergence behaviour, LS3D finds the solution faster than the ICP method, typically in five to six iterations.

Table II gives the numerical results of the co-registration computations. For instance, epoch 0 contained 14 point clouds, resulting in 18·4 million points in total. The 14 point clouds had 24 overlapping pairs whose spatial overlaps on average accounted for 37·7%. The least overlap of those 24 pairs was 3·7% which can still be co-registered successfully by the LS3D matching algorithm. The average of the standard deviations of these 24 pairwise LS3D computations was $\pm 68{\cdot}3\,\mu m$. The final global registration step for this epoch had a standard deviation of $\pm 42{\cdot}4\,\mu m$ which confirmed the accuracy specifications of the sensor. The results of the successive epochs 1, 2, 3 and 4 are comparable.

Interpolation and Surface Generation

Point data is not the standard output of today's structured-light systems. They have to be processed to generate surface models, so that queries and analysis can be conducted. Surface models can be either triangulated irregular networks (TIN) or raster grid forms.

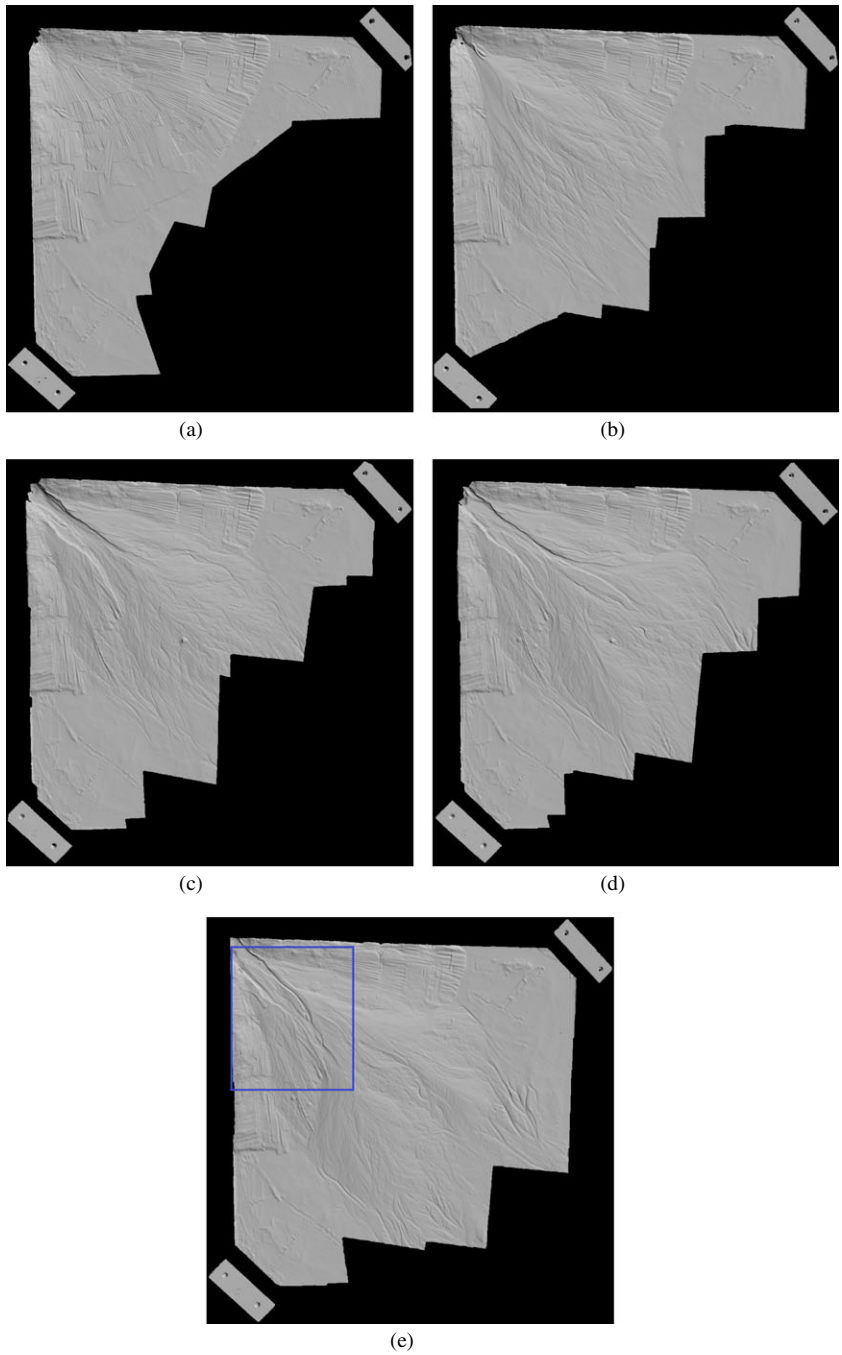

FIG. 5. DEMs of: (a) epoch 0; (b) epoch 1; (c) epoch 2; (d) epoch 3; (e) epoch 4. The spatial extent of Figs. 6(a) and (b) is indicated by the blue rectangle in (e). The T-shaped impressions in the upper right and lower left corners were used for subsequent co-registration.

Raster grids are commonly preferred due to their simplicity and ease of storage, retrieval and processing.

Once the point clouds of each epoch were co-registered, they were re-sampled into a DEM using the SCOP++ interpolation and surface-generation software (version 5.4.2). The point spacing of raster grids was chosen to be 300 µm. Finally, the spatial characteristics of the flume surface at each epoch was represented in five individual DEM layers (Fig. 5).

A close-up view of the upper left area of the epoch 4 DEM (blue rectangle in Fig. 5(e)) is shown in Figs. 6(a) and (b) in image and 3D-model representations, respectively. The red lines and dots in Fig. 6(a) are occlusions and non-cooperative surface parts due to specular reflections in the captured image of the Breuckmann scanner, respectively. The high-resolution DEM in Fig. 6(b), which covers the same spatial extent as Fig. 6(a), allows the detection of small features such as fan, rills, levees and lobes. Fig. 6(c) is an enlargement of the central part (black rectangle) of Fig. 6(b). Both the height of an erosion rill (1·460 mm) and a small lobe (0·061 mm) are still detectable features.

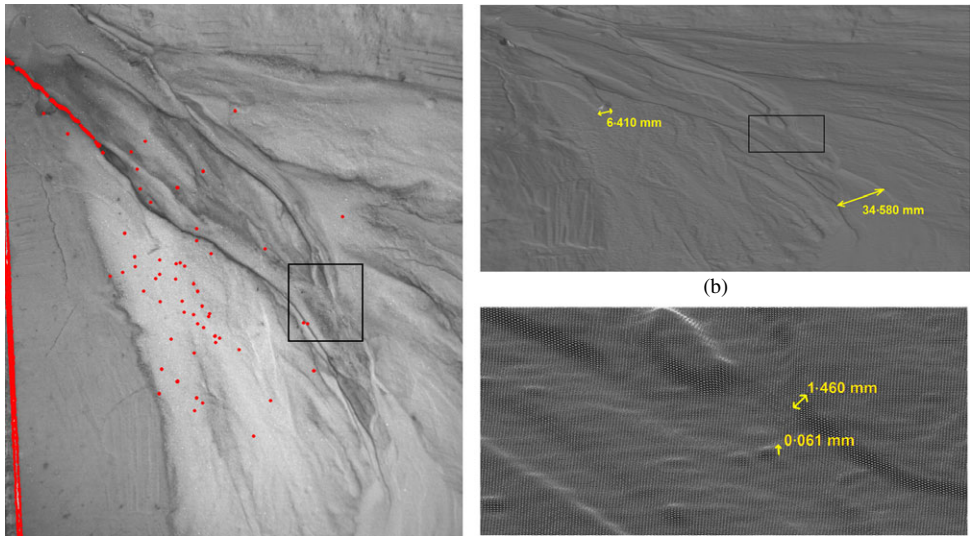

FIG. 6. (a) An image (in nadir view) taken by the internal camera of the Breuckmann scanner of a part of the flume surface in epoch 4 whose extent is given as a blue rectangle in Fig. 5(e). The red lines and dots are occlusions and non-cooperative surface parts due to specular reflections. (b) A shaded 3D (oblique) view of the same area which was rendered from the epoch 4 DEM. (c) A wireframe model of the enlarged view of the black rectangles in (a) and (b).

TABLE III. Numerical results of the co-registrations of the cross-epoch point clouds.

Cross-epochs	*Number of points used (millions)*	*Standard deviation (µm)*	*Computation time (s)*
Epoch 0–1	1·48	137·1	179·3
Epoch 0–2	1·84	109·5	163·7
Epoch 0–3	1·80	117·2	169·8
Epoch 0–4	1·82	86·4	172·6

Co-registration of Epochs

At this point, the five epochs are still not in a common reference frame. In order to perform spatio-temporal epoch analysis, all DEMs have to be transformed into a common spatial coordinate system. Epoch 0 is chosen as the spatial reference datum, and the remaining four DEMs were then co-registered with the reference frame of epoch 0 using the LS3D algorithm. The numerical results are given in Table III.

Since the flume surface has changed in the course of the experiment, only the stable surface parts (see the T-shaped impressions formed by finger marks in the upper right and lower left corners of Figs. 5(a) to (e)) were considered in the co-registration. The standard deviations of these individual co-registrations were between ±86·4 and ±137·1 μm.

Fig. 7 shows the residuals in the co-registration regions of epoch 0 and epoch 3 where the standard deviation was ±117·2 μm. Although bending of the aluminium basin introduced systematic errors, the distribution and pattern of the residuals were still acceptable. The depth direction has almost 100% overlap, whereas the lateral direction has extremely little surface information which are micro structures and roughness along the T-shaped impressions. The LS3D surface-matching method was capable of achieving successful results in this particular example.

3D Comparison and Visualisation

By co-registering the epochs, it is possible to compare the different surface layers to obtain an insight into the spatial and temporal distribution of the sedimentation–erosion pattern evolution. The LS3D surface-matching method was used in a 3D comparison and assessment in order to analyse the change of the surface evolution quantitatively (Akca,

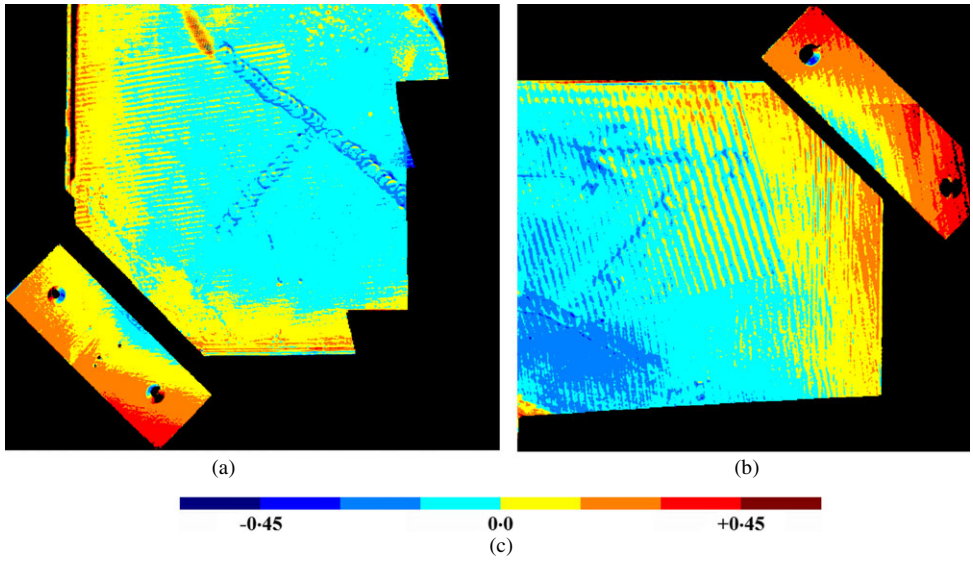

FIG. 7. Residuals of the co-registration computation between epoch 0 and epoch 3. (a) Lower left T-shaped impression and (b) the upper right one. (c) Key to the residual colours, in millimetres, used in (a) and (b).

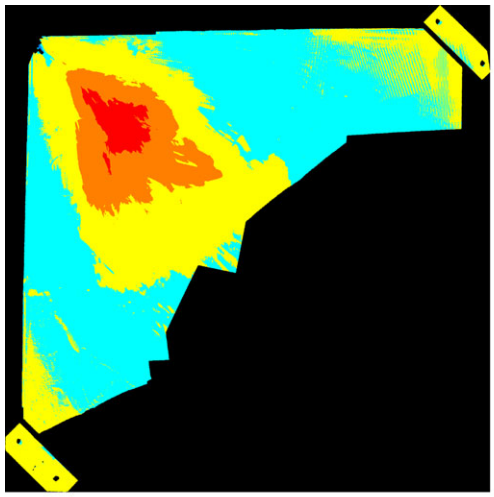

(a)

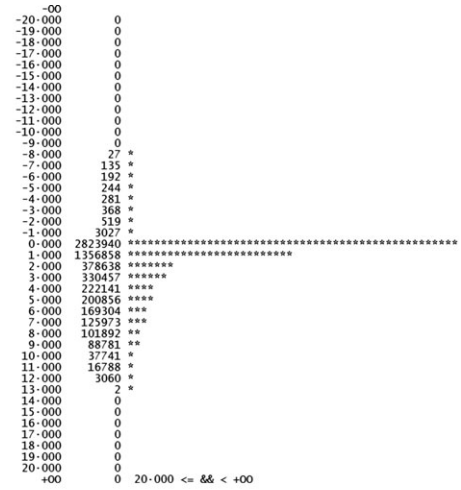

(f)

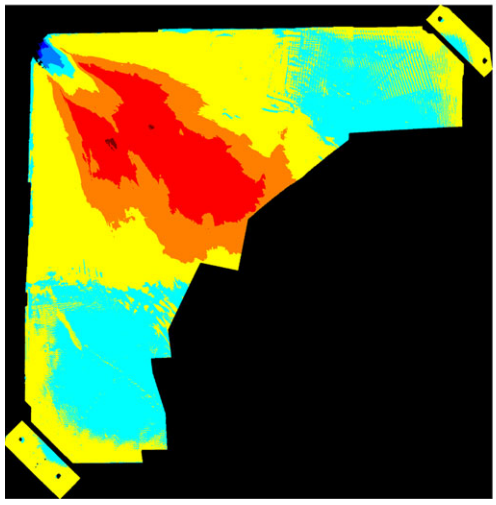

(b)

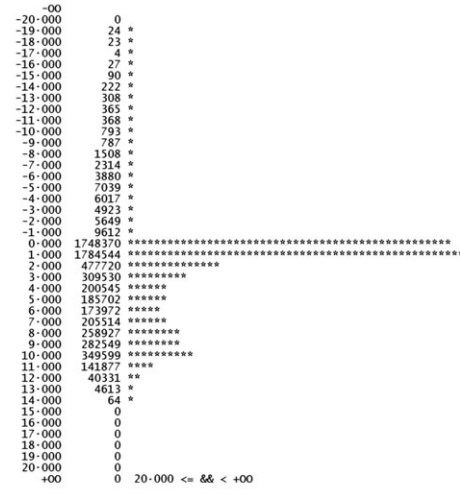

(g)

FIG. 8. Spatial comparisons between the DEMs of: (a) epochs 0–1; (b) epochs 0–2; (c) epochs 0–3; (d) epochs 0–4. (e) Scale of residuals in millimetres. Each comparison is associated with its frequency distribution (histogram) to the right ((f) to (i)). This Figure is continued on the next page.

2010; Akca et al., 2010). It was used to compute only the 3D correspondences without any transformation computation. As the DEM of the initial state (epoch 0) was defined as the datum, the 3D correspondences formed a displacement vector field showing spatial changes (Fig. 8) between the points of the datum DEM (epoch 0) and the conjugate surface elements of the subsequent DEMs (epochs 1, 2, 3 and 4).

Fig. 8(a) shows the major deposition pattern of the first lobe along the diagonal of the flume, which was apparently raised as the sediment was injected (from top left to bottom right). The change in lobe heights attained maximum values of +12·0, +13·1, +13·8 and

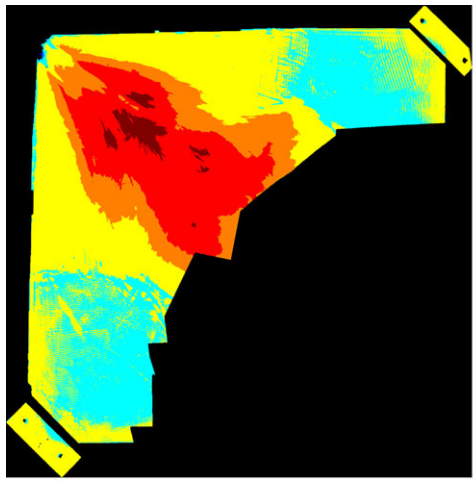

(c)

```
      -00
-20·000        0
-19·000        0
-18·000        0
-17·000        0
-16·000        0
-15·000        0
-14·000        0
-13·000        0
-12·000        3 *
-11·000       28 *
-10·000       84 *
 -9·000      118 *
 -8·000      148 *
 -7·000      124 *
 -6·000      223 *
 -5·000      272 *
 -4·000      479 *
 -3·000      844 *
 -2·000     1491 *
 -1·000     4783 *
  0·000  1552593 **************************************************
  1·000  1505336 ************************************************
  2·000   534745 *****************
  3·000   346948 ***********
  4·000   222792 *******
  5·000   174919 ******
  6·000   178685 ******
  7·000   191923 ******
  8·000   208025 *******
  9·000   274030 *********
 10·000   309223 **********
 11·000   332398 ***********
 12·000   208752 *******
 13·000   100238 ****
 14·000     9966 *
 15·000        0
 16·000        0
 17·000        0
 18·000        0
 19·000        0
 20·000        0
    +00        0  20·000 <= && < +00
```

(h)

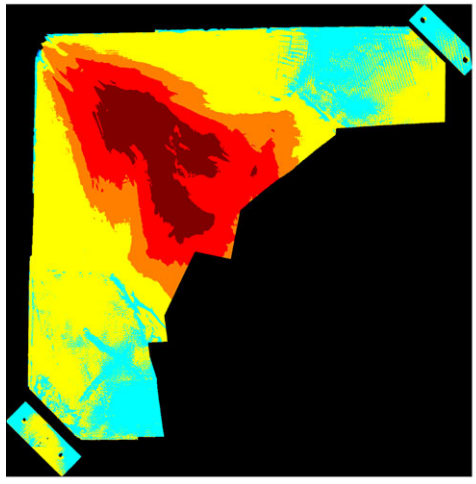

(d)

```
      -00
-20·000        0
-19·000        0
-18·000        0
-17·000        0
-16·000        0
-15·000        0
-14·000        0
-13·000        0
-12·000        0
-11·000        0
-10·000        0
 -9·000        9 *
 -8·000       35 *
 -7·000       88 *
 -6·000      180 *
 -5·000      185 *
 -4·000      486 *
 -3·000      576 *
 -2·000      786 *
 -1·000     6707 *
  0·000  1145650 ************************************
  1·000  1665280 ***************************************************
  2·000   492589 ***************
  3·000   370812 ************
  4·000   286193 *********
  5·000   164031 *****
  6·000   158400 *****
  7·000   157897 *****
  8·000   188291 ******
  9·000   193472 ******
 10·000   211106 *******
 11·000   283150 *********
 12·000   275432 *********
 13·000   265246 ********
 14·000   231831 *******
 15·000    72355 ***
 16·000    25427 *
 17·000     2860 *
 18·000       18 *
 19·000        0
 20·000        0
    +00        0  20·000 <= && < +00
```

(i)

(e)

FIG. 8. Continued from previous page.

+17·0 mm for epochs 1, 2, 3 and 4, respectively. Note the erosion feature close to the inlet location (upper left) of Fig. 8(b), where the water dropping into the flume excavated a small basin; this had a depth of 10 to 14 mm during the second injection. The remaining figures show that the flume experiment (like a real inland delta) is a dominantly depositional feature, with erosion limited to only a few places.

GEOMORPHOLOGICAL ANALYSIS

Slope Analysis

The morphology of the flume experiments' topography can be analysed using local elevation and topographic slope. The latter can be used as a proxy for the dominant land forming processes; for example, a decreasing angle of slope can be due to sedimentation or erosion/abrasion of both fluvial and hillslope processes.

The slope angle can be used to identify steep topographic features such as channel banks and levees. In the experiment these features were approximately 1 to 10 mm in size and were highly heterogeneous, thus requiring sub-millimetre DEMs to be represented accurately. The plots of the local slopes for each epoch are shown in Fig. 9.

To quantify the changes in the surface topography during the evolution of the delta experiment, the average slope $< s >$ was calculated across circular windows of diameter $dr = 5$ cm at different distances d from the inlet along the diagonal. The result $S(d)$ was normalised by dividing by the overall mean slope S_M of the system:

$$S(d) = < s > / S_M. \quad (1)$$

Here S_M is the mean delta slope for a specific epoch, with angles of 16·2°, 16·3°, 15·7°, 15·5° and 14·9° for epochs 0 to 4, respectively.

The normalised mean topographic slope $S(d)$ is a function of the inlet distance d, computed along the entire diagonal of the basin (from top left to bottom right), and is depicted in Figs. 10 and 11. The co-registered DEMs allow the analysis of the change of $S(d)$ for each epoch individually, which is useful in understanding the topographic evolution of fluvial systems.

It can be observed in Fig. 10 that the slope gradually decreases until the base slope of the flume is reached. As $S(d)$ is the ratio of the local mean slope $< s >$ to the overall mean slope S_M, a value of $S(d) = 1{\cdot}0$ implies that the local mean slope is equal to the overall mean slope of that epoch.

The change in the normalised mean topographic slope $S(d)$, which is the subtraction of the respective epoch from the initial state in epoch 0, is plotted in Fig. 11. Clearly, three distinct slope regimes marked in Fig. 11 (also in Figs. 10, 12 and 13) can be identified and compared to local topography and discussed regarding their evolution.

I: A region (5 to 35 cm from the inlet) where the sediment was transported in a well-confined channel with levees. Here, deposition increased with distance from the inlet resulting in a lower average slope compared to the initial condition. This behaviour decreased with distance from the inlet.

II: A region between 35 and 62 cm from the inlet marks the range where the flow started to spread out, distributing the sediment over a larger area of the domain and resulting in a gradual decrease in deposition while keeping a constant transport capacity. This is indicated by a constant change of slope over time in Fig. 11. Figs. 13(b), (c) and (d) also indicate this behaviour.

III: Towards the end of the delta the flow started to deposit its final sediment load onto the base of the flume in finger-like configurations where the small channels were confined by levees. This fact resulted in an increased average slope compared with the initial condition towards the end of the domain (62 to 100 cm).

The mean change of the elevation in successive epochs is depicted as a function of the distance d from the inlet in Fig. 12. The elevation values were again averaged over circular

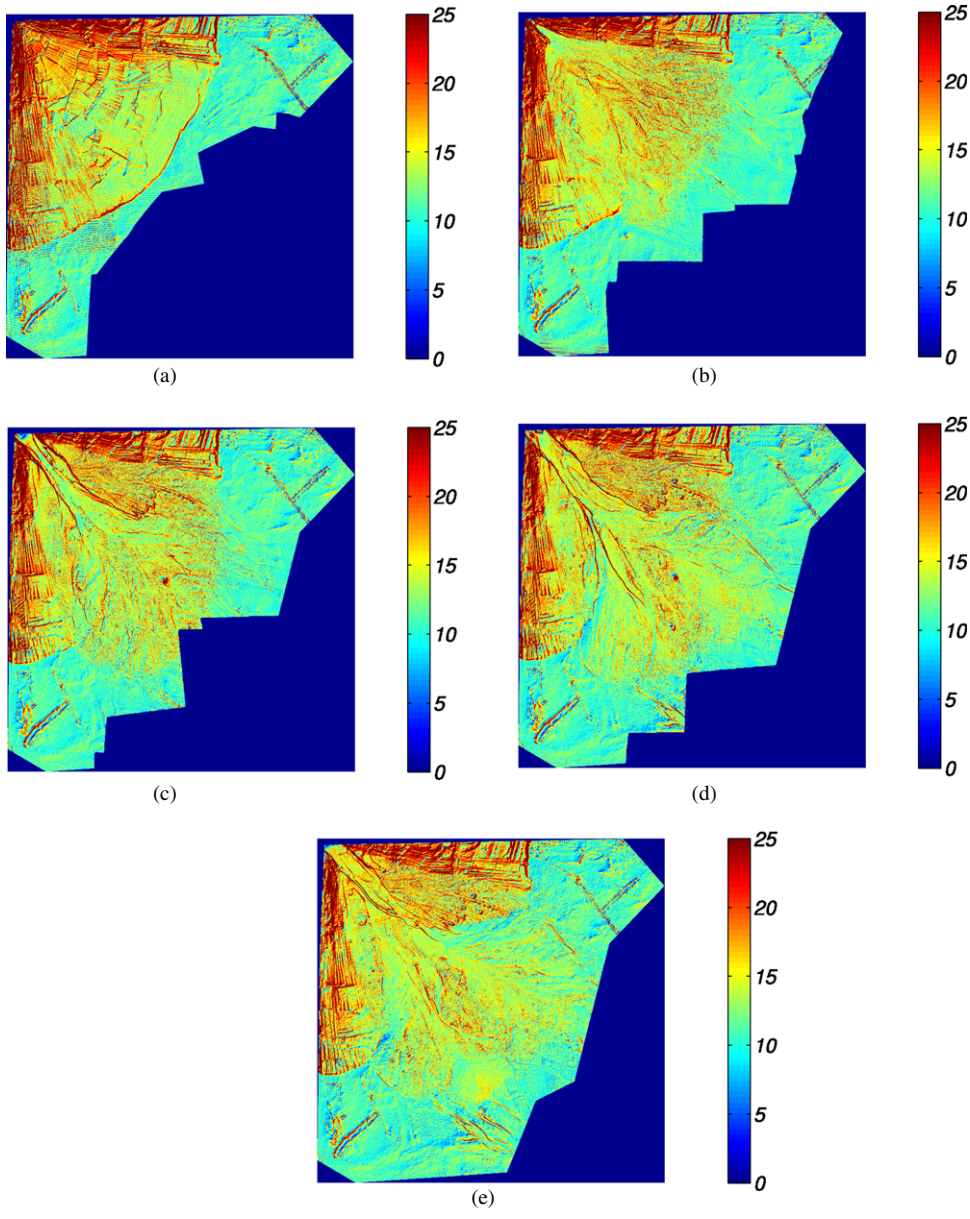

FIG. 9. Slopes for the different epochs of the experiment. (a) Initial conditions (epoch 0); (b) epoch 1; (c) epoch 2; (d) epoch 3; (e) epoch 4. The scale bars indicate the angle of slope in degrees.

windows of diameter $dr = 5$ cm, located along the inlet diagonal d, as was done for the slopes. During epochs 1 and 2 depositions occurred close to the inlet. The lobes of epochs 3 and 4 indicate that little further sediment was deposited at the end of the delta fan. The

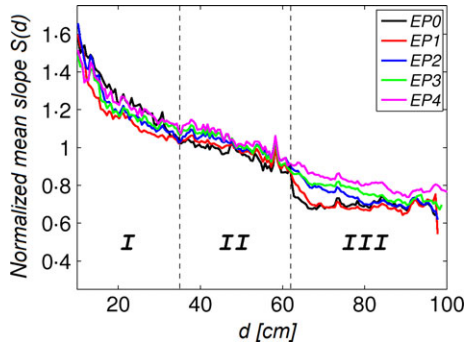

FIG. 10. The normalised mean slope $S(d)$ as a function of the distance d from the inlet along the diagonal. The different epochs are shown as *EP0* to *EP4*. I, II and III are identified as three distinct slope regimes which are discussed in the text.

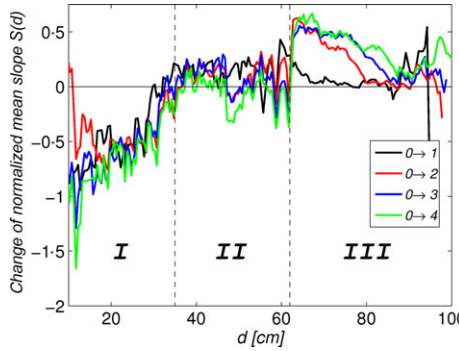

FIG. 11. The change of the normalised mean slope $S(d)$ compared to the initial condition (epoch 0) plotted against distance d from the inlet. The slope $S(d)$ has been averaged over circular windows of diameter dr = 5 cm for different distances d from the inlet and then normalised by dividing by the overall mean slope. Three regions of different slope regimes can be identified: I, II and III.

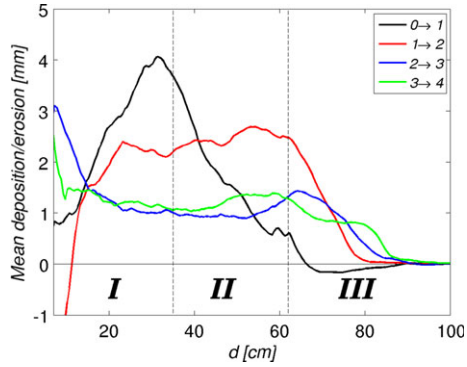

FIG. 12. Mean change of elevation versus distance d from the inlet for successive epochs.

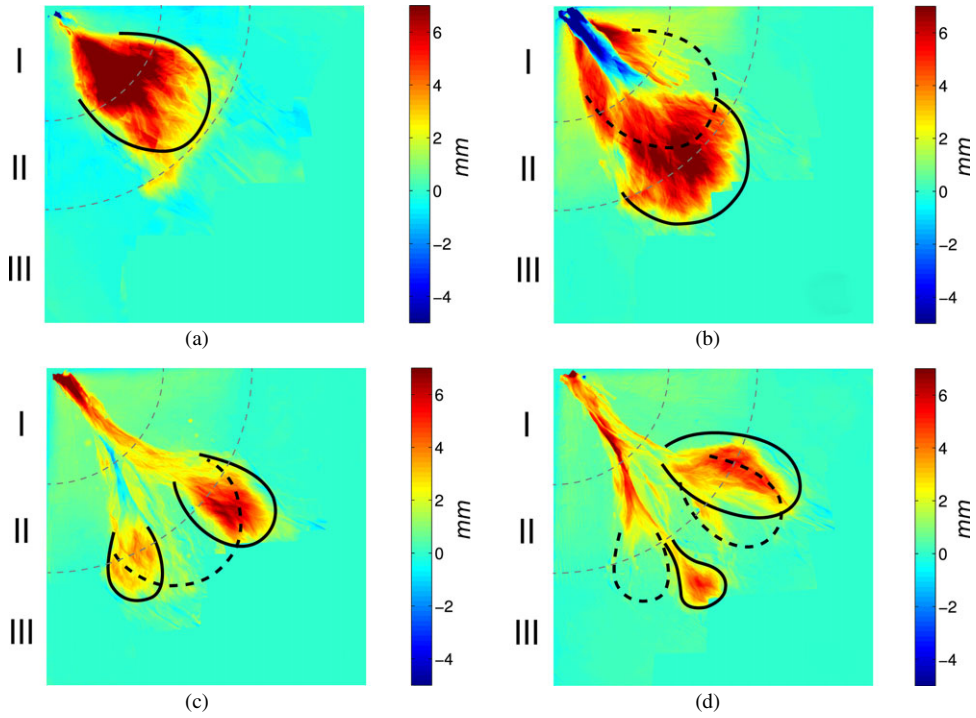

FIG. 13. Spatial distribution of sedimentation and erosion between successive epochs: (a) epochs 1–0; (b) epochs 2–1; (c) epochs 3–2; (d) epochs 4–3. Blues indicate erosion and reds deposition. The current deposition lobe for a given epoch is outlined in black solid lines and the previous lobes are indicated by black dashed lines. The slope regimes I, II and III are outlined as grey dashed arcs.

erosion regime close to the inlet and the deposition region at the far end of the flume can be clearly identified in epochs 3 and 4. The abrupt changes in the inlet zone ($d < 15$ cm) are boundary artefacts which are related to the way the water–sediment mixture was injected into the domain.

Topography Dynamics

The co-registered topographic epoch layers can also be used to analyse the spatial evolution of the deposition pattern over time to gain an insight into the stratigraphy of the delta formation process. The total deposited volume of each epoch can be obtained by simply subtracting the volume of a given DEM from the previous one. The values for the four injections were:

$$\mathrm{V1} = 573\,\mathrm{cm}^3, \mathrm{V2} = 904\,\mathrm{cm}^3, \mathrm{V3} = 614\,\mathrm{cm}^3 \text{ and } \mathrm{V4} = 740\,\mathrm{cm}^3$$

which provides an estimate of the variance of deposition during the different runs.

The common reference frame of the different epochs allows the analysis of the spatial structure of the sedimentation–erosion pattern, as illustrated in Fig. 13. This shows the change in surface elevation between successive epochs. Clearly different lobes and the

switching of the deposition fan between epochs can be identified. The solid lines mark the boundaries of the current epoch's deposition zone and the dashed lines show the boundaries of the previous lobe(s).

During epoch 1 (Fig. 13(a)) the stream mainly deposited its sediment after a short inlet zone, filled up the area and adjusted the initial slope to the transport capacity of the flow. The sediment transport capacity of this so-called *overland flow* was discussed in Julien and Simons (1985).

During the second injection phase (epoch 2) the main flow direction was blocked by the first deposition lobe. Thus, the stream first started to incise a channel in the old lobe before it spread out into a new fan on the left-hand side of the former deposits (Fig. 13(b)). This situation is also apparently visible in Fig. 14 where the epoch 1 and 2 DEMs are superimposed and the channel and the new fan are seen in a 3D view.

The third period (epoch 3) was characterised again by deposition forming a new sediment layer. The main deposition lobe switched to the east of the domain, while a new channel branch eroded through the side walls of the previous lobe. Consequently, a new lobe was formed towards the south of the flume. During this and the following epoch (epoch 4) it can be clearly seen that, initially, sedimentation and erosion occurred only in a well-confined channel until the flow lost its transport capacity and spread out to distribute its deposits over a larger domain forming a deltaic fan (Figs. 13(c) and (d)). The shape of the lobes, which have a thin neck, spread out into a more circular pattern typical of lobes and fans.

CONCLUSIONS

Capturing the dynamics of inland deltas is challenging, as they employ both erosional and depositional processes, competing with each other over the same time scale and land

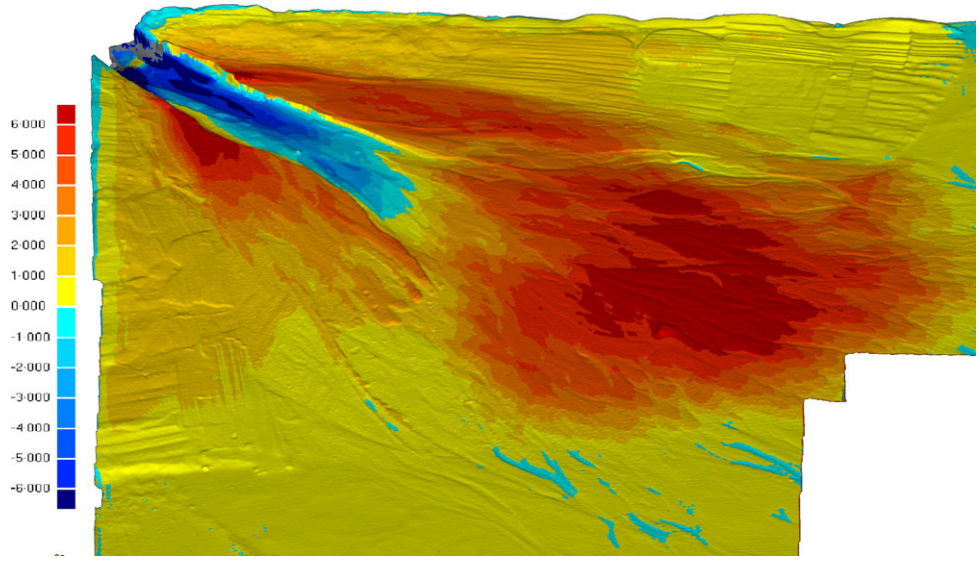

FIG. 14. Overlay of epoch 2–1 DEMs to show erosion and deposition pattern of Fig. 13(b) in a 3D view. The scale bar is in millimetres. Blue colours indicate erosion; yellows and reds indicate deposition. The incised channel, levees and new lobe/fan are visible.

areas. The shape of the deltaic surface is the result of the river's dynamics, its transport capability and the variability of water and sediment input. In this research the formation of an inland delta has been studied using a laboratory-scale flume experiment and high-resolution DEM data analysis. The high-resolution scanning techniques applied allow the measurement of detailed features of the experiment, as well as monitoring of its morphological evolution embodying changes such as branching levees or small erosion patterns inside channels. The main emphasis has been given to geodata acquisition and processing, serving as input to geomorphological analysis. Instrumental and computational aspects have also been outlined.

A Breuckmann 3D scanner has acquired high-quality point-cloud data of the flume surface. The system is capable of measuring surface features with an accuracy of $\pm 50\,\mu m$. Very fine details can be observed, measured and analysed. This investigation shows that active sensing with a coded structured-light system is a mature technology which can be used in laboratory-scale flume experiments.

The co-registered DEMs allow the comparison of the surfaces at different times to gain an insight into the stratigraphic record of the deposition pattern. This led to a more detailed and accurate analysis of the spatio-temporal dynamics of the delta formation process. Lobe switching and channel branching has been observed as in real-world delta settings. The pattern formation mechanisms of the experiment and the resulting morphology are similar to those observed in nature, but on a different scale in both space and time. The presented experimental technique can serve as a tool to understand the interplay between dominant sedimentation processes. Cross analysis of this laboratory flume experiment and the phenomenon of the Okavango Delta in Botswana were discussed in a previous paper by Seybold et al. (2010), which also showed that reduced complexity models of earth-surface evolution require high-quality ground-topography data, preferably in grid representation. The presented methodology fulfils this requirement favourably by adopting: (i) a high-resolution 3D structured-light sensor; (ii) resulting DEMs with $\pm 50\,\mu m$ feature accuracy; and (iii) strict co-registration of topographic data in both spatial and temporal domains.

REFERENCES

Akca, D., 2007. *Least Squares 3D Surface Matching*. Doctoral thesis, Institute of Geodesy and Photogrammetry, ETH Zurich, Switzerland. Mitteilungen Nr. 92. Dissertation No. 17136. 78 pages. http://dx.doi.org/10.3929/ethz-a-005461765 [Accessed: 20th January 2016].

Akca, D., 2010. Co-registration of surfaces by 3D least squares matching. *Photogrammetric Engineering & Remote Sensing*, 76(3): 307–318.

Akca, D., 2012. 3D modeling of cultural heritage objects with a structured light system. *Mediterranean Archaeology and Archaeometry*, 12(1): 139–152.

Akca, D., 2013. Photogrammetric monitoring of an artificially generated shallow landslide. *Photogrammetric Record*, 28(142): 178–195.

Akca, D., Freeman, M., Sargent, I. and Gruen, A., 2010. Quality assessment of 3D building data. *Photogrammetric Record*, 25(132): 339–355.

Babault, J., Bonnet, S., Crave, A. and Driessche, J. V. D., 2005. Influence of piedmont sedimentation on erosion dynamics of an uplifting landscape: an experimental approach. *Geology*, 33(4): 301–304.

Berger, C., Schulze, M., Rieke-Zapp, D. and Schlunegger, F., 2010. Rill development and soil erosion: a laboratory study of slope and rainfall intensity. *Earth Surface Processes and Landforms*, 35(12): 1456–1467.

Besl, P. J. and McKay, N. D., 1992. A method for registration of 3D shapes. *IEEE Transactions on Pattern Analysis and Machine Intelligence*, 14(2): 239–256.

Bokulich, A., 2013. Explanatory models versus predictive models: reduced complexity modeling in geomorphology. Part 2 in *EPSA11 Perspectives and Foundational Problems in Philosophy of Science* (Eds. V. Karakostas and D. Dieks). Springer, Heidelberg, Germany. 510 pages: 115–128.

BONNET, S., 2009. Shrinking and splitting of drainage basins in orogenic landscapes from the migration of the main drainage divide. *Nature Geoscience*, 2(11): 766–771.

BONNET, S. and CRAVE, A., 2003. Landscape response to climate change: insights from experimental modeling and implications for tectonic versus climatic uplift of topography. *Geology*, 31(2): 123–126.

BRASINGTON, J., VERICAT, D. and RYCHKOV, I., 2012. Modeling river bed morphology, roughness, and surface sedimentology using high resolution terrestrial laser scanning. *Water Resources Research*, 48(11): W11519. DOI:10.1029/2012WR012223.

BRODU, N. and LAGUE, D., 2012. 3D terrestrial lidar data classification of complex natural scenes using a multi-scale dimensionality criterion: applications in geomorphology. *ISPRS Journal of Photogrammetry and Remote Sensing*, 68: 121–134.

BUCKLEY, S. J., ENGE, H. D., CARLSSON, C. and HOWELL, J. A., 2010. Terrestrial laser scanning for use in virtual outcrop geology. *Photogrammetric Record*, 25(131): 225–239.

CHANDLER, J. H., 2010. Close range morphological measurement for the earth sciences. *Photogrammetric Record*, 25(131): 223–224.

CHANDLER, J. H., SHIONO, K., RAMESHWAREN, P. and LANE, S. N., 2001. Measuring flume surfaces for hydraulics research using a Kodak DCS460. *Photogrammetric Record*, 17(97): 39–61.

CHANDLER, J. H., BUFFIN-BÉLANGER, T., RICE, S., REID, I. and GRAHAM, D. J., 2003. The accuracy of a river bed moulding/casting system and the effectiveness of a low-cost digital camera for recording river bed fabric. *Photogrammetric Record*, 18(103): 209–223.

CHEN, Y. and MEDIONI, G., 1992. Object modelling by registration of multiple range images. *Image and Vision Computing*, 10(3): 145–155.

GENG, J., 2011. Structured-light 3D surface imaging: a tutorial. *Advances in Optics and Photonics*, 3(2): 128–160.

GESSESSE, G. D., FUCHS, H., MANSBERGER, R., KLIK, A. and RIEKE-ZAPP, D. H., 2010. Assessment of erosion, deposition and rill development on irregular soil surfaces using close range digital photogrammetry. *Photogrammetric Record*, 25(131): 299–318.

GRUEN, A. and AKCA, D., 2005. Least squares 3D surface curve matching. *ISPRS Journal of Photogrammetry and Remote Sensing*, 59(3): 151–174.

HENG, B. C. P., CHANDLER, J. H. and ARMSTRONG, A., 2010. Applying close range digital photogrammetry in soil erosion studies. *Photogrammetric Record*, 25(131): 240–265.

HODGE, R., BRASINGTON, J. and RICHARDS, K., 2009. *In situ* characterization of grain-scale fluvial morphology using terrestrial laser scanning. *Earth Surface Processes and Landforms*, 34(7): 954–968.

HOHENTHAL, J., ALHO, P., HYYPPÄ, J. and HYYPPÄ, H., 2011. Laser scanning applications in fluvial studies. *Progress in Physical Geography*, 35(6): 782–809.

HOYAL, D. C. J. D. and SHEETS, B. A., 2009. Morphodynamic evolution of experimental cohesive deltas. *Journal of Geophysical Research*, 114(F2): F02009. DOI:10.1029/2007JF000882.

HÜRLIMANN, M., MCARDELL, B. W. and RICKLI, C., 2015. Field and laboratory analysis of the runout characteristics of hillslope debris flows in Switzerland. *Geomorphology*, 232: 20–32.

JOUANNIC, G., GARGANI, J., CONWAY, S. J., COSTARD, F., BALME, M. R., PATEL, M. R., MASSE, M., MARMO, C., JOMELLI, V. and ORI, G. G., 2015. Laboratory simulation of debris flows over sand dunes: insights into gully-formation (Mars). *Geomorphology*, 231: 101–115.

JULIEN, P. Y. and SIMONS, D. B., 1985. Sediment transport capacity of overland flow. *Transactions of the American Society of Agricultural Engineers ASAE*, 28(3): 755–762.

KIRBY, R. P., 1991. Measurement of surface roughness in desert terrain by close range photogrammetry. *Photogrammetric Record*, 13(78): 855–875.

KRAAL, E. R., VAN DIJK, M., POSTMA, G. and KLEINHANS, M. G., 2008. Martian stepped-delta formation by rapid water release. *Nature*, 451(7181): 973–976.

LIANG, M., VOLLER, V. R. and PAOLA, C., 2015. A reduced-complexity model for river delta formation – Part 1: modeling deltas with channel dynamics. *Earth Surface Dynamics*, 3: 67–86. DOI:10.5194/esurf-3-67-2015.

MARTIN, J., SHEETS, B., PAOLA, C. and HOYAL, D., 2009. Influence of steady base-level rise on channel mobility, shoreline migration, and scaling properties of cohesive experimental delta. *Journal of Geophysical Research*, 114(F3): F03017. DOI:10.1029/2008JF001142.

MEREL, A. P. and FARRES, P. J., 1998. The monitoring of soil surface development using analytical photogrammetry. *Photogrammetric Record*, 16(92): 331–345.

MILAN, D. J., HERITAGE, G. L. and HETHERINGTON, D., 2007. Application of a 3D laser scanner in the assessment of erosion and deposition volumes and channel change in a proglacial river. *Earth Surface Processes and Landforms*, 32(11): 1657–1674.

Paola, C. and Leeder, M., 2011. Environmental dynamics: simplicity versus complexity. *Nature*, 469(7328): 38–39.
Pyle, C. J., Richards, K. S. and Chandler, J. H., 1997. Digital photogrammetric monitoring of river bank erosion. *Photogrammetric Record*, 15(89): 753–764.
Remondino, F., 2011. Heritage recording and 3D modeling with photogrammetry and 3D scanning. *Remote Sensing*, 3(6): 1104–1138.
Rieke-Zapp, D. H. and Nearing, M. A., 2005. Digital close range photogrammetry for measurement of soil erosion. *Photogrammetric Record*, 20(109): 69–87.
Rieke-Zapp, D. H., Beer, A., Turowski, J. M. and Campana, L., 2012. In situ measurement of bedrock erosion. *International Archives of Photogrammetry, Remote Sensing and Spatial Information Sciences*, 39(B5): 429–433.
Salvi, J., Fernandez, S., Pribanic, T. and Llado, X., 2010. A state of the art in structured light patterns for surface profilometry. *Pattern Recognition*, 43(8): 2666–2680.
Seybold, H. J., Molnar, P., Singer, H. M., Andrade, J. S., Herrmann, H. J. and Kinzelbach, W., 2009. Simulation of birdfoot delta formation with application to the Mississippi Delta. *Journal of Geophysical Research*, 114(F3): F03012. DOI:10.1029/2009JF001248.
Seybold, H. J., Molnar, P., Akca, D., Doumi, M., Cavalcanti Tavares, M., Shinbrot, T., Andrade, J. S., Kinzelbach, W. and Herrmann, H. J., 2010. Topography of inland deltas: observations, modeling, and experiments. *Geophysical Research Letters*, 37(8): L08402. DOI:10.1029/2009GL041605.
Stojic, M., Chandler, J. H., Ashmore, P. and Luce, J., 1998. The assessment of sediment transport rates by automated digital photogrammetry. *Photogrammetric Engineering & Remote Sensing*, 64(5): 387–395.
Turowski, J. M., Lague, D., Crave, A. and Hovius, N., 2006. Experimental channel response to tectonic uplift. *Journal of Geophysical Research*, 111(F3): F03008. DOI:10.1029/2005JF000306.
Welch, R. and Jordan, T. R., 1983. Analytical non-metric close-range photogrammetry for monitoring stream channel erosion. *Photogrammetric Engineering & Remote Sensing*, 49(3): 367–374.
Wilson, A. and Lavé, J., 2013. The legacy of impact conditions in morphometrics of percussion marks on fluvial bedrock surfaces. *Geomorphology*, 186: 174–180.
Zhang, Z., 1994. Iterative point matching for registration of freeform curves and surfaces. *International Journal of Computer Vision*, 13(2): 119–152.

Résumé

Un modèle de compléxité réduite, qui simule le processus de formation d'un delta intérieur, a été développé dans une précédente étude. Les résultats ont été comparés et validés dans le cadre d'une expérience en laboratoire qui est décrite dans cet article. Un delta intérieur expérimental est formé, et sa topographie sujette à l'érosion est mesurée au moyen d'un scanner 3D à lumière structurée. La méthode LS3D de recalage et comparaison par moindres carrés est utilisée pour l'orientation et pour comparer, dans l'espace et dans le temps, les données acquises à différentes dates. Une précision spatiale de l'ordre de ±50 μm (1/20 000) est obtenue. Une série de modèles numériques de terrain (MNT) de haute qualité est produite et l'évolution spatio-temporelle du delta intérieur est surveillée et analysée, en termes de pente et de dynamique topographique, dans les MNT consécutifs. La combinaison du scanner à haute resolution avec les techniques de recalage de haute précision permet d'étudier en détail la variabilité spatio-temporelle des motifs de dépôt sédimentaire pour l'analyse géomorphologique.

Zusammenfassung

In einer vorangegangenen Studie wurde ein sogenanntes "reduced complexity" Computermodel zur Simulation von Inlanddeltas vorgestellt, und die Resultate mit Experimenten und Feldmessungen verglichen. Hier vertiefen wir die Analyse des Experiments, welches die Erosions- und Ablagerungsprocesse der Deltadynamik auf Laborscalen nachbildet. Die Änderung der Oberflächentopographie wurde mit Hilfe eines hochauflösenden "structured light" Scanner gemessen. Zur Kombination und Co-registrierung der einzelnen Oberflächenteilstücke kam der LS3D Algorithmus zum Einsatz, welcher es erlaubt Oberflächenmodelle mit einer Präzission von ±50 μm (1/20 000) zu verschiedenen Zeiten des Experiments zu erzeugen. Diese hochaufgelösten

und co-registrierten Oberflächenmodelle können dazu verwendet werden Veränderungen in der Topographie in Raum und Zeit zu beschreiben, was dabei hilft die Dynamik der zu grunde liegenden geomorphischen Prozesse besser zu verstehen.

Resumen

En un estudio previo se ha desarrollado un modelo de complejidad reducida, que simula el proceso de formación en el interior-delta fluvial. Los resultados se han comparado y validado con un experimento de laboratorio. Este trabajo explica con detalle el experimento de laboratorio en el que se genera un delta interior experimental y, usando un escáner 3D de luz estructurada, se mide la topografía erosionada. Se usa el co-registro 3D de mínimos cuadrados y el método LS3D tanto para la alineación como para comparar datos espacial y temporalmente. Se alcanza una precisión espacial alrededor de ±50 micras (1/20 000). Se han generado una serie de modelos de elevación digital de alta calidad (DEM) monitorizándose y analizándose, en términos de dinámica de pendiente y topografía, la evolución espacio-temporal del delta interior mediante las capas DEM consecutivas. La combinación de escaneo de alta resolución junto con técnicas de co-registro de alta precisión permite la investigación de los detalles de la variabilidad espacio-temporal de patrones de sedimentación y deposición que se han utilizado para el análisis geomorfológico.

摘要

在前面的研究中,已采用降阶的复杂模型来模拟河流内陆三角洲形成过程,并与实验室实验的结果进行了比较和验证。本文阐述了实验室验证中,制作了试验性的内陆三角洲,其侵蚀地形采用结构光三维扫描仪进行测量。采用三维最小二乘配准方法用来进行不同时间空间的侵蚀状态的配准,空间精度达到*±50 μm (1/20 000)*。利用序列高质量的数字高程模型,从坡度和地形动态方便,对内陆三角洲的侵蚀过程进行了监测和分析。组合高分扫描和高精度配准技术可用来调查地貌分析中沉积模式的连续时空变化细节。